AGU PUBLICATIONS

JGR

Journal of Geophysical Research: Atmospheres

RESEARCH ARTICLE

10.1002/2013JD021141

Key Points:
- Statistical scaling exponents are inferred from tower-based observations
- Water vapor scaling exponents are reported for tower-based observations
- In situ observations largely confirm previous remote sensing results

Correspondence to:
K. G. Pressel,
pressel@caltech.edu

Citation:
Pressel, K. G., W. D. Collins, and A. R. Desai (2014), The spatial scale dependence of water vapor variability inferred from observations from a very tall tower, *J. Geophys. Res. Atmos.*, *119*, 9822–9837, doi:10.1002/2013JD021141.

Received 4 NOV 2013
Accepted 10 JUL 2014
Accepted article online 15 JUL 2014
Published online 28 AUG 2014

The spatial scale dependence of water vapor variability inferred from observations from a very tall tower

Kyle G. Pressel[1,2,3], William D. Collins[2,3], and Ankur R. Desai[4]

[1]Division of Geological and Planetary Sciences, California Institute of Technology, Pasadena, California, USA, [2]Climate Sciences Department, Lawrence Orlando Berkeley National Laboratory, Berkeley, California, USA, [3]Department of Earth and Planetary Science, University of California, Berkeley, California, USA, [4]Department of Atmospheric and Ocean Sciences, University of Wisconsin-Madison, Madison, Wisconsin, USA

Abstract Recent studies have established that atmospheric water vapor fields exhibit spatial spectra that take the form of power laws and hence can be compactly characterized by scaling exponents. The power law scaling exponents have been shown to exhibit substantial vertical variability. In this work, Taylor's frozen turbulence hypothesis is used to infer the first-order spatial structure function and generalized detrended fluctuation function scaling exponents for scales between 1 km and 100 km. Both methods are used to estimate the Hurst exponent (H) using 10 Hz time series of water vapor measured at 396 m altitude from an Ameriflux tower in Wisconsin. Due to the diurnal cycle in the boundary layer height at the 396 m observational level, H may be estimated for both the daytime convective mixed layer and the nocturnal residual layer. Values of $H \approx \frac{1}{3}$ are obtained for the convective mixed layer, while values of $H > \frac{1}{2}$ apply in the nocturnal residual layer. The results are shown to be remarkably consistent with a similar analysis from satellite-based observations as reported in Pressel and Collins (2012).

1. Introduction

There has been a recent intensification of interest in questions regarding the scale dependence of statistical moments of atmospheric fields. Initially, questions regarding statistical scale dependence were motivated by a desire for theoretical understanding of the energetics and physics of atmospheric flows [e.g., *Charney*, 1971]. More recent work has been motivated by the need to develop parameterizations that link the statistical properties of spatial scales resolvable by numerical models with statistical properties of scales that are, as yet, unresolvable [e.g., *Larson et al.*, 2001].

At present, there is no unified theory of atmospheric dynamics across spatial scales that is sufficiently general to provide a theoretical basis for making the connection between resolved and unresolved scales on theoretical grounds alone. In the absence of a purely theoretical approach, there are two alternate viable approaches to gain insight into this problem. First, numerical approaches based upon simulations of large spatial domains can be performed with sufficient resolution that the scale dependence of statistics can be investigated across the grid-scale to subgrid-scale transition. Second, empirical approaches can exploit observational data sets spanning an appropriate range of scales. Of the two approaches, the second approach has been the one frequently adopted [e.g., *Cho et al.*, 2000; *Kahn and Teixeira*, 2009; *Kahn et al.*, 2011; *Pressel and Collins*, 2012; *Fischer et al.*, 2012, 2013; KT09; PC12].

There are two primary limitations on the numerical simulation approach that stem from finite constraints on computational resources. First, the scale dependence of statistical moments computed from any practicable numerical simulation may be affected by subgrid-scale parameterizations as well as by numerical dissipation at scales up to several times the grid resolution [e.g., *Skamarock*, 2004; *Kahn et al.*, 2011]. A second, and perhaps less frequently considered, issue is that the scale dependence of statistics computed from limited area domains may be sensitive to the domain size [e.g., *de Roode et al.*, 2004; *Bretherton et al.*, 2005]. In either case, the limitations follow from the fact that current numerical simulations can only account for a small portion of the total number of degrees of freedom of the real atmosphere.

While empirical approaches are not limited by a constraint on the total number of degrees of freedom, they are subject to other limitations in spatiotemporal extent and resolution. (Note that this is a fundamentally different resolution limitation from those in numerical models, as observations made at a particular

resolution are correctly influenced by processes occurring at all scales.) Moreover, observations from remote sensing platforms are subject to limitations on vertical accuracy resulting from their retrieval algorithms (PC12 added abbreviation).

Much of the recent interest in the scale dependence of atmospheric fields has focused on the power law scaling of water vapor variance spectra and structure functions [e.g., *Cho et al.*, 2000; *Kahn et al.*, 2011; *Fischer et al.*, 2012, 2013; KT09; PC12]. One of the reasons for the renewed interest is the direct applicability of these scale-dependent characterizations to the parameterization of cloud variability in atmospheric models [e.g., *Cusack et al.*, 1999; *Larson et al.*, 2012]. Based upon previous studies using in situ aircraft [*Cho et al.*, 2000; KT09], satellite [*Kahn et al.*, 2011; KT09; PC12], and airborne lidar [*Fischer et al.*, 2012, 2013] observations, there is a growing consensus that the extratropical water vapor spectral scaling exponents exhibit substantial and consistent vertical variability at scales between 1 km and 500 km. In particular, extratropical spectra are shown to exhibit steeper scaling in the free troposphere than in the lower troposphere. The Hurst exponent (H), which can be either directly approximated or can be deduced from the power law scaling exponents reported in the aforementioned observational studies, offers a compact description of statistical properties of spatial correlations in the observed field. Hurst exponents can take values between 0 and 1. Values of $H < 0.5$ are caused by the presence of anticorrelated or switching behavior between sequential increments taken at a particular scale, while values of $H > 0.5$ indicate that sequential increments are correlated suggesting the presence of long-range correlations. Hurst exponents computed from subtropical and midlatitude spectra reported by KT09, *Kahn et al.* [2011], PC12, and *Fischer et al.* [2012, 2013] cluster around $H = \frac{1}{3}$ in proximity to the planetary boundary layer (PBL) and increase with altitude so that $H > \frac{1}{2}$ in the free troposphere. As a result, the water vapor fields in the two regimes are distinguished by anticorrelated spatial variability in the PBL and long-range horizontal correlations in the free troposphere.

Both PC12 and *Fischer et al.* [2012, 2013] argue that the difference between free tropospheric and PBL exponents are the result of fundamentally different transport and mixing phenomena. They have argued that the absence of long-range correlations, as indicated by $H < \frac{1}{2}$ in the PBL, arises from small-scale convective transport that can rapidly mix water vapor arising from surface sources in the vertical direction. *Fischer et al.* [2012] suggest that the observed $H \approx \frac{1}{3}$ behavior results from an upscale transfer from buoyant convection. In the free troposphere, PC12 propose that the long-range correlations are formed as a result of largely two-dimensional transport and mixing of water vapor that has been advected away from spatially localized source regions. This explanation is supported by the findings of *Fischer et al.* [2012], who note that their observations made over middle and southwest Europe often show that at upper levels air which has been transported over long distances from the Atlantic is characterized by spectra with larger scaling exponents.

However, the previous studies have often been limited by relatively small sample sizes for analyses based upon aircraft observations and by uncertainties in vertical profile accuracy, together with relatively coarse horizontal and vertical resolution of the retrievals in analyses based upon satellite observations. These limitations have motivated the work presented here in which we characterize the spatial scale dependence of water vapor variability inferred from time series of observations collected from the 396 m level of the WLEF television broadcast tower in Wisconsin. The use of tower-based observations permits analysis of statistical scaling from composite spectra with much larger sample sizes than are readily available from aircraft surveys and with higher vertical accuracy than is typical of satellite data. Furthermore, the height of the tower permits observations of both the daytime convective mixed layer and nocturnal residual layer at various points in the diurnal cycle of the boundary layer. Having observations in these two regimes permits us to characterize the scaling of water vapor spectra when the water vapor field is being either vertically mixed by buoyant convection or horizontally transported by quasi-two-dimensional large-scale flows.

This article will begin by discussing the statistical methods used to compute spatial spectra from the observed time series. Then the instrumentation at the WLEF site will be discussed and used to characterize the diurnal cycle of the PBL in order to identify when the 396 m level of the WLEF tower is located in the daytime convectively mixed layer or in the nocturnal boundary layer residual layer. Finally, the computed Hurst exponents will be compared to previous results.

2. Statistical Methodology

Two methods are used in this study to investigate the statistical scale dependence of water vapor by estimating Hurst exponents H_q of the qth-order generalized structure functions from measurements from the

WLEF tower. In previous studies, H_q has been estimated using either structure functions or variance spectra, both of which assume stationarity of the observed data set. The observational data set used here is likely to exhibit nonstationarity resulting from the diurnal cycle in boundary layer height and other properties. An alternative approach to estimating H_q is to use detrended fluctuation analysis in order to minimize the effects of statistical nonstationarity on the computed exponents. Both structure function analysis and detrended fluctuation analysis are applied to the WLEF time series. In order to facilitate comparisons with previous studies, the structure function and detrended fluctuation analysis methodologies will be used to estimate H_1 based on the scaling of first-order statistics. We note that H_1 is frequently referred to as the Hurst exponent which we will denote as H.

2.1. Computation of Structure Function Scaling Exponents

The structure function algorithm operates on a data series ϕ_k that is N elements in length and for which the distance in time or space between sequential ϕ_k is constant. The distance between sequential ϕ_k is denoted ΔX. The value of the qth-order generalized structure function $S_q(s)$ at a scale s can then be computed directly by

$$S_q(s) = \frac{1}{N-n} \sum_{i=1}^{N-n} \left| \phi_i - \phi_{i+n} \right|^q \tag{1}$$

where the scale s is an integer multiple n of the separation ΔX. Structure function values $S_q(s)$ can then be computed for a range of scales s.

For a portion of the structure function exhibiting scaling, the power law behavior of $S_q(s)$ can be written mathematically as

$$S_q(s) \propto s^{H_q} \tag{2}$$

where H_q is the generalized Hurst exponent.

The scaling behavior of the qth-order structure function $S_q(s)$ can be determined by the goodness of fit of the linear regression of $\log S_q(s)$ versus $\log s$. The slope parameter resulting from the linear fit is an estimate of H_q. The Hurst exponent H, which we focus on in this study, is equal to the first-order generalized Hurst exponent; therefore,

$$H = H_1. \tag{3}$$

2.2. Computation of Detrended Fluctuation Function Scaling Exponents

Detrended fluctuation analysis was originally described by *Peng et al.* [1994] as a means of assessing statistical scale invariance in statistically nonstationary data series. The methodology relies on the computation of a function that relates the behavior of second-order statistics to an arbitrary scale. Detrended fluctuation analysis has been applied to numerous natural systems including the spatial structure of clouds [e.g., *Ivanova et al.*, 2000], climate records [e.g., *Koscielny-Bunde et al.*, 1998; *Ivanova and Ausloos*, 1999; *Talkner and Weber*, 2000], and hydrology [e.g., *Matsoukas et al.*, 2000; *Li and Zhang*, 2007]. The detrended fluctuation analysis method was extended to relate the behavior of other orders of statistics to an arbitrary scale by *Kantelhardt et al.* [2002] with the development of multifractal detrended fluctuation analysis. Applications of multifractal detrended fluctuation analysis to natural systems have included hydrology [e.g., *Zhang et al.*, 2008], meteorology [e.g., *Kavasseri and Nagarajan*, 2005], and climate [e.g., *Varotsos et al.*, 2006]. In this study, multifractal detrended fluctuation analysis (MF-DFA) is used in order to facilitate comparison to first-order structure function scaling exponents.

While a description of the MF-DFA algorithm is given in *Kantelhardt et al.* [2002] and *Leung* [2010], for completeness we include a similar description here. The algorithm operates on a data series ϕ_k that is N elements in length and begins by computing the profile $Y(i)$ of the series ϕ_k

$$Y(i) = \sum_{k=1}^{i} \left[\phi_k - \langle \phi \rangle \right], i = 1, \ldots, N \tag{4}$$

where $\langle \phi \rangle$ is the arithmetic mean of ϕ_k. Note that $Y(i)$ is also a series of length N. The profile $Y(i)$ is then divided into $N_s \equiv \text{int}(N/s)$ nonoverlapping segments of length s. In order to span an entire series $Y(i)$ whose

length is not an integer multiple of s, the series is also divided starting at the opposite end such that there are total of $2N_s$ segments of length s. Least squares regression is used to calculate the local trend for each of the $2N_s$ segments of $Y(i)$ of length s (in this study linear least square regression is used to calculate the local trend). The least squares curve fit for the νth segment is denoted by $y_\nu(i)$. For each segment ν, $\nu = 1, ..., N_s$ the variance is computed by

$$F^2(s,\nu) = \frac{1}{s}\sum_{i=1}^{s}\left\{Y\left[(\nu-1)s+i\right] - y_\nu(i)\right\}^2 \tag{5}$$

and for each segment ν, $\nu = N_s + 1, ..., 2N_s$ the variance is computed by

$$F^2(s,\nu) = \frac{1}{s}\sum_{i=1}^{s}\left\{Y\left[N-(\nu-1)s+i\right] - y_\nu(i)\right\}^2 \tag{6}$$

Averaging over all $2N_s$ segments of length s yields the value of qth-order fluctuation function at scale s as

$$F_q(s) \equiv \left\{\frac{1}{2N_s}\sum_{\nu=1}^{2N_s}\left[F^2(s,\nu)\right]^{\frac{q}{2}}\right\}^{\frac{1}{q}} \tag{7}$$

Equations (4)–(7) are then repeated for a range of scales s.

The scaling behavior of the fluctuation function $F_q(s)$ can be determined by analysis of log-log plots of $F_q(s)$ to identify segments that are approximately linear and therefore exhibit scaling (i.e., power law behavior). For each scaling portion, the power law behavior of $F_q(s)$ can be written mathematically as

$$F_q(s) \propto s^{H_q+1} \tag{8}$$

where H_q is the generalized Hurst exponent. Within each portion that exhibits scaling, the scaling exponent can be determined by performing a least squares linear regression of the logarithm of $F_q(s)$ versus logarithm of s.

2.3. Taylor's Frozen Turbulence Hypothesis

In order to investigate the spatial scale dependence of water vapor from an observed time series, spatial separations must be inferred from discrete temporal samples. *Taylor*'s [1935] frozen turbulence hypothesis is commonly used to approximate spatial correlations from temporal correlations. The accuracy of the approximation is dependent on the properties of the particular flow of interest [*Pope*, 2000]. If the approximation holds exactly, then it asserts the exact equivalence between Eulerian space and Eulerian time spectra [*Lappe and Davidson*, 1963]. Numerous studies find support for the application of Taylor's hypothesis across a wide range of space and time scales [e.g., *Gifford*, 1956; *Gossard*, 1960; *Lappe and Davidson*, 1963; *Brown and Robinson*, 1979; *L'vov et al.*, 1999]. Additionally, Taylor's hypothesis has been used in most studies that have investigated the scale dependence of atmospheric variability through aircraft and fixed point observations [e.g., *Nastrom and Gage*, 1985; *Gage and Nastrom*, 1986; *Cho et al.*, 1999a, 1999b, 2000; *Wood and Hartmann*, 2006].

The frozen turbulence hypothesis posits that a variable $\phi\left(t_i\right)$, observed at discrete times t_k beginning at an initial time t_0, can be assumed to have been observed at spatial points x_k given by

$$x_k = x_0 + \bar{U}t_k \tag{9}$$

where x_o is the spatial position at the initial time t_0 and $\bar{U}$ is the mean wind speed. If $x_0 = 0$, then

$$\phi\left(x_k\right) = \phi\left(\bar{U}t_k\right) \tag{10}$$

Therefore, the range of spatial scales that can be computed from a given time series are dependent on the temporal length of the time series and the mean wind speed $\bar{U}$ during the period of observation.

3. Observational Infrastructure and Paradigm

The 447 m WLEF television broadcast tower is located near Park Falls, Wisconsin (45.95°N, 90.27°W) at a tower base elevation of 472 m above sea level [*Berger et al.*, 2001]. The surrounding forest ecosystem is characterized by a largely heterogeneous mixture of mature deciduous forests in the uplands, wetlands that are populated by mixtures of deciduous and coniferous trees in lower elevations, and more recently logged areas that are largely composed of younger aspen trees [*Davis et al.*, 2003]. The peak forest canopy height is approximately 25 m, and the tower is surrounded by a clearing with a radius of approximately 200 m. A detailed description of the forest ecology surrounding the WLEF site is given in *Mackay et al.* [2002]. The topographical relief is characterized by rolling hills, with lowland to upland elevation differences of approximately 20 m over spatial scales of approximately 200 m [*Davis et al.*, 2003]. Despite the heterogeneity of the surrounding ecosystem, given the spatiotemporal scales considered in this study, the surrounding ecosystem is assumed to be directionally homogeneous.

The WLEF tower observational platform has been designed to synthesize measurements taken at multiple tower heights to provide observed time series of vertical profiles of mean CO_2 mixing ratios, CO_2 fluxes, and sensible and latent heat fluxes. The observed fluxes are computed from the observed variables by eddy covariance techniques [*Berger et al.*, 2001]. Computation of the aforementioned fluxes using eddy covariance techniques necessitates high-frequency observations of sonic virtual temperatures, specific humidities, CO_2 mixing ratios, and three-dimensional wind velocities. These raw observed variables and computed fluxes at the 30 m, 122 m, and 396 m levels serve as the primary empirical bases for this study.

The micrometeorological instrumentation located at each of the three tower levels used in support of this study includes sonic anemometers (ATI, Inc. Type K Sonic anemometer), which measure three-dimensional wind velocities and sonic virtual temperatures with 10 Hz frequency, as well as Li-Cor, Inc. 6262 CO_2/H_2O high-frequency infrared gas analyzers which provide 10 Hz measurements of water vapor and CO_2 mixing ratios [*Berger et al.*, 2001]. The Li-Cor high-frequency infrared gas analyzers are located at the base of the tower. The analyzers sample air drawn continuously through 0.009 m inner diameter tubes that connect each of these instruments at ground level to its corresponding observational level [*Berger et al.*, 2001]. Transport of sampled air through the tubes leads to dissipation of small-scale gradients, although the bias incurred through this mechanism should not have appreciable affects at the scales considered in this study. A detailed description of the flux computation methodology is given in *Berger et al.* [2001] and *Zhao et al.* [1997].

The study relies on diurnal variations in the structure of the planetary boundary layer to make observations of water vapor mixing ratios within both the convective mixed layer and the nocturnal residual layer. Observations from the 396 m tower level are used to probe the water vapor field, while observations at the 30 m, 122 m, and 396 m levels are used to characterize the state of the boundary layer. This combination of data is sufficient to characterize the spatial scale dependence of water vapor variability in the convective mixed layer and nocturnal residual layer from the mesoscale down to the 100 m scale characteristic of individual cloud elements.

While the WLEF tower offers a long-term climatology of observations spanning over a decade, this study is limited to data during the summer seasons (June, July, and August) of 2007 to June 2011 for several reasons. First, limiting the analysis to the summer season affords the opportunity to investigate the diurnal variation of the scale dependence of water vapor statistics when the diurnal variations in the dynamics of the boundary layer are maximized due to the large daily cycle in insolation. Second, due to the exponential dependence of saturation vapor pressure on temperature and the presence of a nonfrozen land surface, the large resulting values of water vapor mixing ratios during the warm season ensure that temporal fluctuations in the water vapor field are larger than the instrument sensitivity.

3.1. Planetary Boundary Layer Characterization

The analytical strategy employed in this study depends critically on the existence of data series measured entirely within the nocturnal residual layer or within the convective mixed layer. Furthermore, in order to maximize the range of scales over which scale-dependent variability can be assessed, it is necessary to maximize the length of the data series. In the course of this study, several algorithms have been developed to automatically categorize segments of the WLEF time series into regimes either within or above the boundary layer. However, evaluation showed that categorization of the data into nocturnal residual layer and

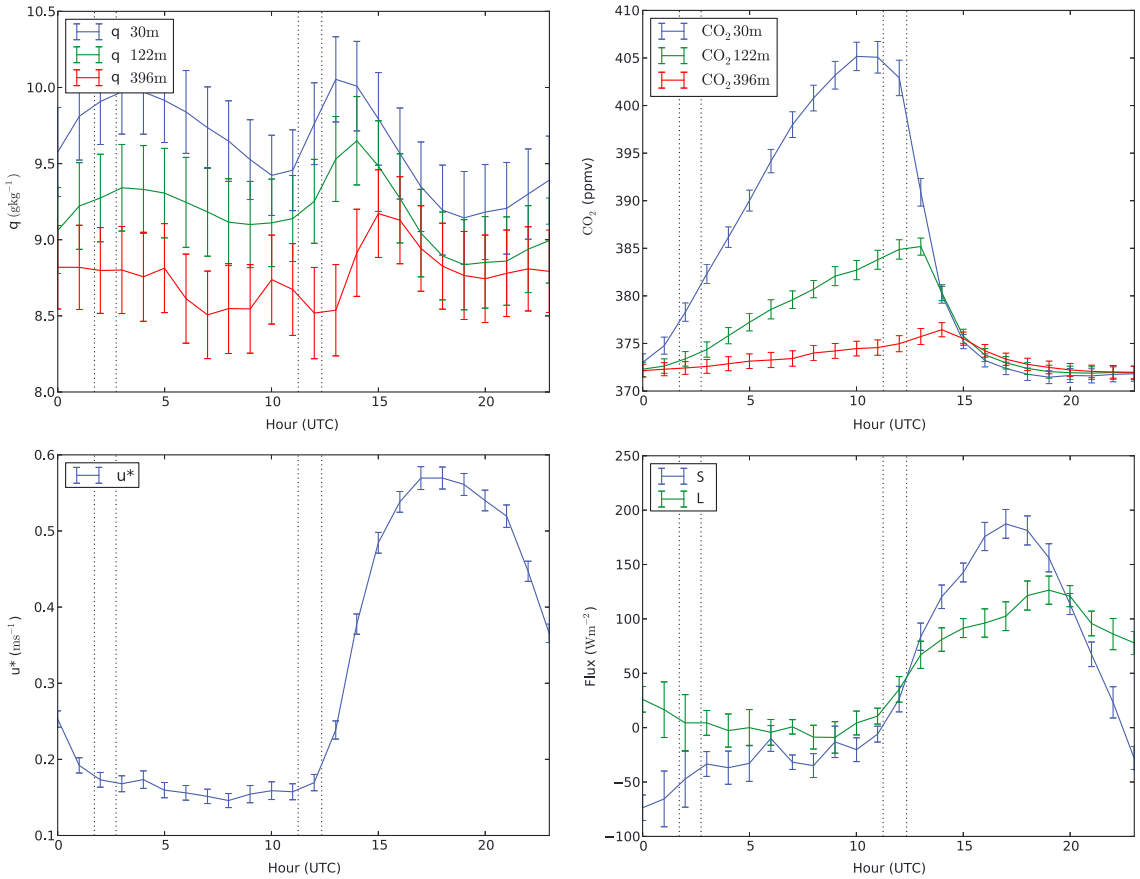

Figure 1. The mean diurnal cycle of (top left) water vapor mixing ratio (g kg^{-1}), (top right) CO_2 mixing ratio (ppmv), (bottom left) friction velocity (m s^{-1}), and (bottom right) latent *L* and sensible *S* heat flux (W m^{-2}). The means are computed for the June, July, and August months between June 2007 and June 2011. The vertical dotted lines indicate the range of sunset (≈2 h UTC) and sunrise times (≈12 UTC). The sensible and latent heat fluxes are only shown for the 396 m level. Vertical error bars are used to indicate the standard error estimate of the means.

convective boundary layer regimes with fixed starting and end points provided the most direct and easily justifiable method. In order to determine the starting and ending points for subsetting the data, an objective analysis of the mean diurnal cycle of $[CO_2]$, sensible heat flux *S*, latent heat flux *L*, and friction velocity u^* at the 396 m level of the WLEF tower has been conducted to identify the mean onset and termination times of the nocturnal residual layer and convective boundary layer regimes. The results of this analysis will be shown later in this section.

3.1.1. The Mean Diurnal Cycle of Water Vapor

Figure 1 (top left) shows the mean diurnal cycle of water vapor mixing ratio *q* as observed at the 396 m, 122 m, and 30 m levels of the WLEF tower. The diurnal cycle of *q* at 396 m is characterized by a relatively small diurnal variation with a difference between maximum and minimum values of the mean diurnal cycle of about 0.5 g kg^{-1}. The absence of a substantial mean diurnal cycle in water vapor mixing ratio is not surprising since the mixing ratio is a conserved variable in the absence of evaporation or condensation and since the mixing ratio does not depend on temperature in contrast to humidity measures such as relative humidity.

There is some evidence of a minimum in *q* near sunrise and a relatively broad maximum that occurs throughout the daylight hours. In comparison to the other observational levels, the 396 m level tends to be drier than the 30 m and 122 m levels at night. At 30 m and 122 m, there is a more pronounced maximum in *q* closely following sunrise than at 396 m, and the local time when the maximum occurs increases with increasing height. The correlation between the time and altitude of the maxima is the first empirical evidence of a time-dependent evolution of the boundary layer, such that at night the top of the stable boundary layer lies below the 396 m level and during the day the 396 m level lies within the convective boundary layer.

3.1.2. The Mean Diurnal Cycle of Vertical CO_2 Differences

The mean diurnal cycle of CO_2 concentration, hereafter $[CO_2]$, is shown in Figure 1 (top right). The maximum value of $[CO_2]$ occurs just prior to sunrise at 30 m and just after sunrise at the 122 m and 396 m levels, with a similar delay in the occurrence of the daily maximum value with height as was seen for q. The minimum value of $[CO_2]$ in the mean diurnal cycle occurs a few hours prior to sunset. The large diurnal cycle is primarily a result of substantial time-dependent surface sources and sinks of $[CO_2]$ associated with aerobic microbial respiration and photosynthesis, respectively. While these substantial sources and sinks of $[CO_2]$ that lead to the observed diurnal evolution are interesting in their own right, they also provide a means of interpreting the diurnal evolution of the boundary layer and in particular of estimating the position of the top of the planetary boundary layer [*Yi et al.*, 2001].

Understanding the connection between the position of the top of the planetary boundary layer relative to the 396 m tower level and the observed vertical differences in $[CO_2]$ concentration requires understanding the role of the biological processes that are the prominent sources and sinks of $[CO_2]$ as well as transport processes that transport $[CO_2]$ vertically in the atmosphere [*Yi et al.*, 2001]. The dominant biological processes that control the vertical gradient of $[CO_2]$ are the consumption of $[CO_2]$ by photosynthesis, which to first order is controlled by the amount of photosynthetically active radiation, and the release of $[CO_2]$ as a by-product of aerobic respiration by soil microbes, which is largely controlled by the soil temperature. Deep soil temperature remains relatively constant throughout the diurnal cycle, and therefore the release of $[CO_2]$ from soils also remains relatively constant. Conversely, due to the substantial diurnal variation in photosynthetically active radiation, the uptake of $[CO_2]$ by plants also undergoes a large daily cycle. The stably stratified boundary layer serves as an impediment to the vertical transport and mixing of $[CO_2]$ at night, thereby allowing a large $[CO_2]$ concentration to build up near the ground level giving rise to large vertical gradients in $[CO_2]$ as is evident in Figure 1 (top right). During the daytime, turbulent mixing dissipates the vertical gradients in $[CO_2]$ that formed during the night. The uptake of $[CO_2]$ by plants is sufficiently rapid that by 15 h UTC the $[CO_2]$ concentration at 396 m exceeds that at 30 m despite the vigorous mixing occurring in the daytime convective boundary layer.

Based on these fluid dynamical and biological processes, *Yi et al.* [2001] have identified the existence of this diurnal variation in $[CO_2]$ gradients at multiple tower levels as a basis for identifying decoupling between particular tower levels and the surface. Based on the methodology shown in *Yi et al.* [2001], Figure 1 (top right) suggests that the 396 m level begins decoupling from the surface beginning just prior to sunset when the difference in $[CO_2]$ concentration between the 30 m and 396 m levels begins to grow. It then begins to recouple with the surface by roughly 15 h UTC when the vertical gradient has been largely diminished.

3.1.3. The Mean Diurnal Cycle of u^* at 396 m

The mean diurnal cycle of the friction velocity u^* is shown in Figure 1 (bottom left) for the 396 m tower level. The friction velocity u^* is defined as

$$u^* = \left(\overline{u'w'}\right)^{\frac{1}{2}} \tag{11}$$

where u' and w' are the vertical and horizontal fluctuating velocity components. The friction velocity is related to the vertical flux of horizontal momentum and therefore the vertical shear stress [e.g., *Holton*, 2004]. The mean diurnal cycle is characterized by nearly a factor of 3 increase in u^* between daytime and nighttime conditions that is associated with larger vertical fluxes of momentum associated with the convective mixed layer relative to the more laminar conditions observed at night. The variation in u^* over the daytime portion of the diurnal cycle is larger than the variation over the nighttime portion. This is related to the variability of the turbulence intensity in association with changes in the surface sensible heat fluxes. In comparison to the vertical gradient in $[CO_2]$ shown in Figure 1 (top right), the transition between the daytime and nighttime regimes for u^* begins slightly later. Based upon these observations, the mean diurnal cycle of u^* suggest that the daytime convective mixed layer likely envelopes the 396 m level by 15 h UTC and then transitions to the more laminar nighttime residual layer by 4 h UTC.

The mean diurnal variation of sensible S and latent L heat fluxes is shown in Figure 1 (bottom right). The functional shape of the diurnal cycle of S and L is fairly similar to that seen for u^* and is characterized by maximum values in the day and minimum values at night. Both S and L exhibit a crossover from the nighttime to daytime regimes that occurs at roughly the same time as was observed for u^*. Perhaps more interesting is

Table 1. Starting and Ending Time for Analysis Periods[a]

Length (h)	Night Start (UTC)	Night End (UTC)	Day Start (UTC)	Day End (UTC)
3	6	9	18	21
5	5	10	17	22
7	4	11	16	23
9	3	12	15	24

[a]The night and day start are the starting times in UTC of the analysis periods for the nighttime residual layer and daytime within mixed layer periods, respectively. The night and day end are the ending times in UTC of the analysis periods for the nighttime residual layer and daytime within mixed layer periods, respectively.

the somewhat smaller diurnal range in L and the pronounced flattening of the daytime portion of the diurnal cycle relative to S, both of which are consistent with the perceived stationarity of the mean water vapor time series shown in Figure 1 (top left). The diurnal cycle evident in S and L shown in Figure 1 (bottom right) largely agree with the transition between the convective mixed layer and residual layer suggested by the diurnal cycles of CO_2 and u^*.

3.1.4. Selection of Analysis Periods

As previously discussed, this analysis of the mean diurnal cycle in tower observations has been motivated by a need to determine the longest subsets of the diurnal cycle that can be identified as being entirely within either the convective mixed layer or the residual layer. All of the observed variables indicate that a transition between residual layer and daytime convective mixed layer conditions at the 396 m level occurs near sunrise and that the opposite transition, between daytime and nighttime conditions, occurs just before sunset. In order to most unambiguously represent the two regimes that occur at the 396 m level, subsets of daily time series are selected that are approximately centered on the temporal midpoint of the two regimes. These correspond to midpoint times of 7.5 h UTC and 19.5 h UTC for the residual layer and convective mixed layer regimes, respectively. In order to determine the sensitivity of the results to the length of the analysis, the analysis periods are varied. Table 1 gives the starting and ending times of the periods of analysis used in this study.

3.2. Algorithmic Implementation

The implementation of the structure function and detrended fluctuation algorithms to analyze the WLEF time series is relatively straightforward. The only deviations from the direct implementation of the algorithms given in section 2.1 pertain to the removal of erroneous observations from the time series, cloud masking, normalization, and the use of Taylor's frozen turbulence hypothesis to convert temporal scales to spatial scales.

Time series values that are flagged as erroneous are removed from the time series. The presence of cloud at the 396 m level could lead to errors in the water vapor measurements due to wetting of the sampling tube inlet that would likely lead to overestimation of the mixing ratio. The presence of cloud at the 396 m level can be identified by an increase in the number of sonic anemometer measurements flagged as erroneous due to the effects of cloud droplets in the beam path, and the erroneous values are used to mask cloudiness at the 396 m level.

The structure function and detrended fluctuation analysis algorithms have been applied to the WLEF 396 m water vapor mixing ratio observations during the time subsets of each diurnal cycle given in Table 1. This yields one structure function and one detrended fluctuation function for each of the nocturnal residual layer and convective mixed layer subsets. Averaging is then performed in three steps. First, Taylor's frozen turbulence hypothesis is used to convert the time scale of the structure function and detrended fluctuation function to a length scale using the mean wind speed computed for the period of analysis. This is performed for each residual layer and convective mixed layer structure function and detrended fluctuation function using the mean horizontal wind speed computed for each. As a result, each residual layer and convective mixed layer structure function and detrended fluctuation function is defined over a unique set of discrete scales. Second, the spatial structure functions and detrended fluctuation functions are normalized by their value at the scale closest to 0.5 km. Third, discrete spatial scales for all functions are then binned into logarithmically spaced bins, and the mean of each bin is computed.

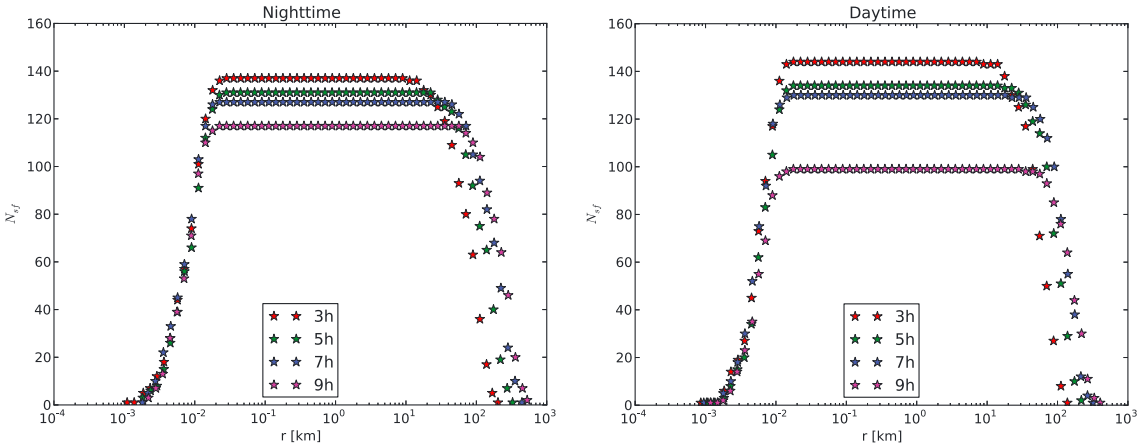

Figure 2. The number of samples of daily structure functions and detrended fluctuation functions N_{sf} included in the computation of the mean for all length scales r. Colored symbols denote the length of analysis periods (see Table 1).

The final output of the algorithm is a single mean structure and detrended fluctuation function of length scale for each of the residual layer and mixed layer periods given in Table 1. The normalization, performed in the second step of the averaging procedure described above, ensures that each structure function and detrended fluctuation function is weighted equally in the average. The normalization does not change the slope of the log-log structure function or detrended fluctuation function.

As a result of the variability of the mean horizontal wind speed, not all length scales are sampled with equal frequency. Figure 2 shows plots of the number of times N_{sf} each length scale bin is sampled during the June 2007 to June 2011 analysis period. The decrease in N_{sf} at the smallest and largest scales occurs because these scales are only sampled on the calmest and windiest days, respectively. Despite the less frequent sampling at very large and small scales, it is clear that there is a range of length scales spanning several decades that are sampled by all structure functions.

4. Results

The methods for constructing structure and detrended fluctuation functions that were described in the previous section have been used to analyze the scale dependence of variability in observations of water vapor mixing ratio from the WLEF tower. Two sets of results are shown for the analyses of both structure and detrended fluctuation functions. In the first set of results, the structure and detrended fluctuation functions are truncated at a scale equal to one quarter of their temporal length. In the notation used in section 2, this is equivalent to truncation at a scale equal to $N_s/4$. The reason for this truncation is to ensure that at each scale the computed values of the structure functions and detrended fluctuation functions are sufficiently statistically robust estimates. The second set of results does not employ truncation, and hence the functions are defined over a larger range of scales. While there is some danger in interpreting the results at larger scales which may not be robustly estimated for any given daily structure function, it is likely that much of this danger is ameliorated in the spatial binning and averaging process. In the next part of the results section, the computed structure functions and detrended fluctuation functions are shown alongside the best fitting power laws for each so that qualitative features of the structure functions and detrended fluctuation functions can be considered. Quantitative assessment of the scaling behavior of the structure functions and detrended fluctuation functions is reserved until the end of the section, where it is reported in tabular form.

4.1. Results With Truncation at $N_s/4$

Figure 3 (top right and top left) depicts the first-order structure functions for the nocturnal residual layer and daytime convective mixed layer. The structure functions for all subset lengths are shown in each plot. In both the nocturnal residual layer and convective mixed layer cases the linearity at scales from 1 km to 100 km is indicative of power law behavior. Linear least squares lines for scales between 1 km and 100 km are plotted for each of the structure functions. The coincidence of the least squares lines suggests that the structure functions exhibit similar power law behavior.

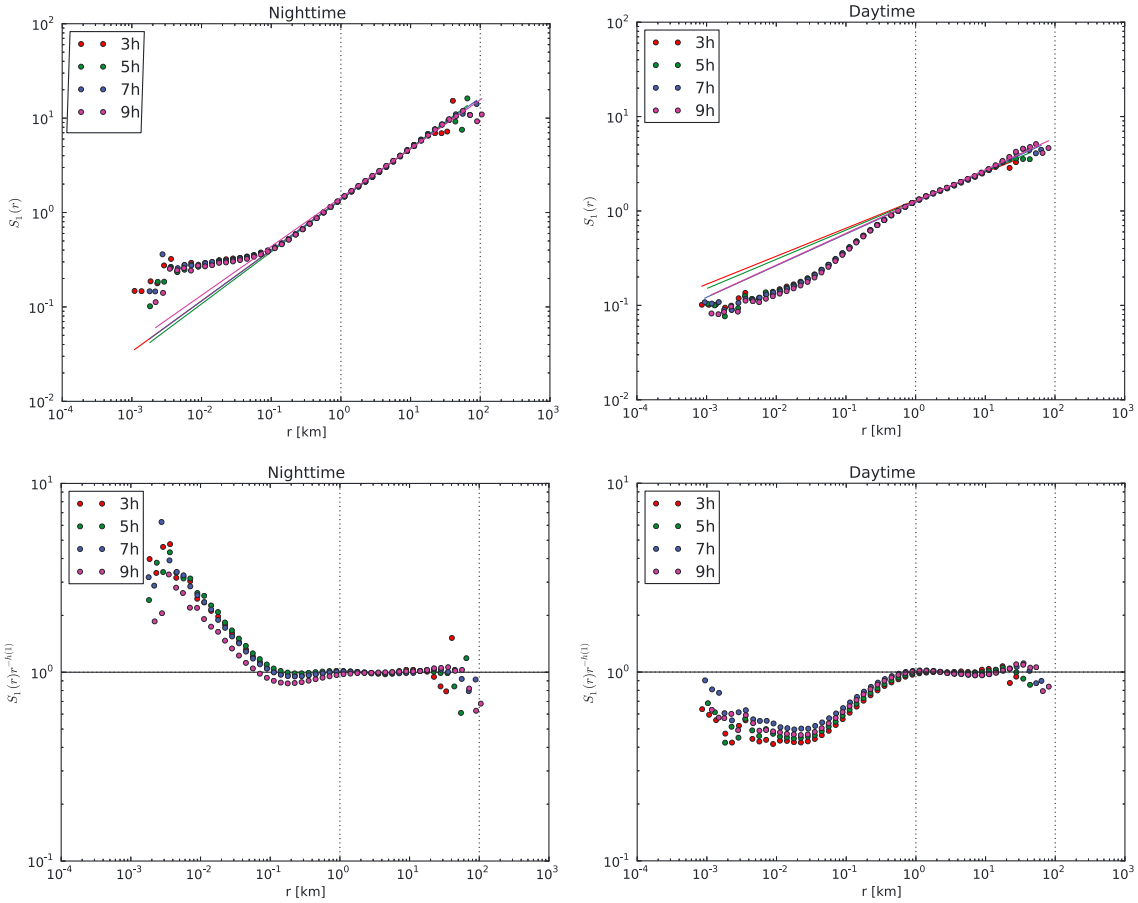

Figure 3. Plots of the first-order structure functions $S_1(r)$ truncated at $N_s/4$ for (top left) nocturnal residual layer and (top right) daytime convective mixed layer regimes. Each curve has been normalized by its value at $r = 10$ km. The best fitting power laws are shown as solid lines. Vertical dotted lines indicate the least squares fitting region. The normalized first-order structure function $S_1(r)/r^H$ truncated at $N_s/4$ for (bottom left) nocturnal residual layer and (bottom right) daytime convective mixed layer regimes. Colored symbols denote the length of analysis periods as defined in Table 1.

If a structure function S_1 exhibits power law dependence on r with scaling exponent H, then plots of S_1/r^H should appear as constant functions of r. Plots of S_1/r^H, where H is determined by the least squares fits shown in Figure 3 (top left and top right), are shown in Figure 3 (bottom left and bottom right). The near constant function behavior of S_1/r^H at scales between 1 km and 100 km confirms the power law behavior evident in Figure 3 (bottom left and bottom right). At large scales, there appears to be some divergence from power law behavior, but this is likely due to undersampling at these large scales as suggested by Figure 2.

Figure 4 depicts the detrended fluctuation functions truncated at $N_s/4$. The general behavior of the detrended fluctuation functions is similar to that seen for the structure functions shown in Figure 3, with clear power law scale dependence between 1 km and 100 km and departure from simple scaling at small scales during both daytime and nighttime. The departures at small scales are likely related to the damping of small-scale gradients associated with transport through the sampling tube. The least squares power law fits that are shown in Figure 4 suggest that the power law behavior is largely independent of the length of the analysis interval.

Plots of F_1/r^{H+1} are shown in Figure 4 (bottom left and bottom right) and should be interpreted similarly to the plots of S_1/r^H shown in Figure 3 (bottom left and bottom right). The constant function of r behavior between 1 km and 100 km again confirms the power law behavior at these scales. The break from power law behavior of F_1/r^H at large scales is reduced relative to S_1/r^H.

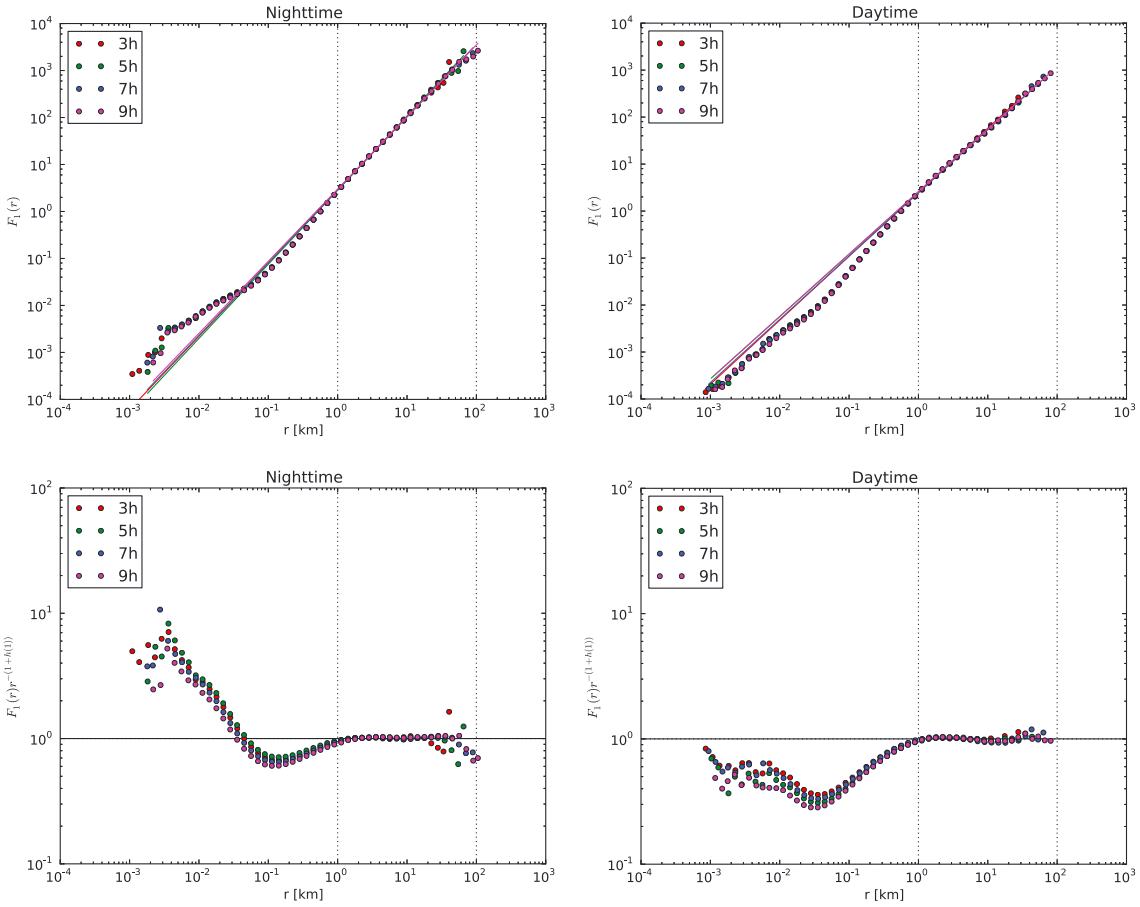

Figure 4. Plots of the detrended fluctuation functions $F_1(r)$ truncated at $N_s/4$ for (top left) nocturnal residual layer and (top right) convective mixed layer regimes. Each curve has been normalized by its value at $r = 10$ km. The best fitting power laws are shown as solid lines. Vertical dotted lines indicate the least squares fitting region. The normalized detrended fluctuation functions $F_1(r)/r^{H+1}$ truncated at $N_s/4$ for (bottom left) nocturnal residual layer and (bottom right) daytime convective mixed layer regimes. Colored symbols denote the length of analysis periods as defined in Table 1.

4.2. Results With No Truncation

Figure 5 shows the convective mixed layer and residual layer structure functions without truncation. Results for the nocturnal residual layer are shown in Figure 5 (top left) and show clear evidence of the presence of power law behavior at scales between 1 km and 100 km. At the largest scales for each subset length, there is some evidence of a concave departure of the structure functions from this power law, although given the infrequency with which these scales are sampled (e.g., Figure 2) and the questionable robustness of structure function estimates at these scales, any physical interpretation of the flattening is questionable.

Unlike the untruncated residual layer case which is largely consistent with its truncated counterpart, there are substantial differences evident between the truncated and untruncated convective mixed layer structure functions. The most prominent difference between the truncated and untruncated convective mixed layer results is that the power law behavior is less distinct in the nontruncated case. This deviation from power law behavior is best observed by noting the larger variation in the structure functions about their best fit lines.

Figure 5 (bottom left and bottom right) depicts plots of S_1/r^H as were shown in Figure 3 (bottom left and bottom right) for the truncated structure functions. The plots shown in Figure 5 largely confirm the existence of power law behavior for the residual layer cases between 1 km and 100 km and the apparent departure from power law behavior for the convective mixed layer cases across the same range of scales.

Figure 6 depicts the convective mixed layer and residual layer detrended fluctuations without truncation. The nontruncated detrended fluctuation function results bear much similarity to the truncated results for both the nocturnal residual layer and convective mixed layer cases. This similarity was not as apparent for the truncated and nontruncated structure functions and suggests that some portion of the departure from

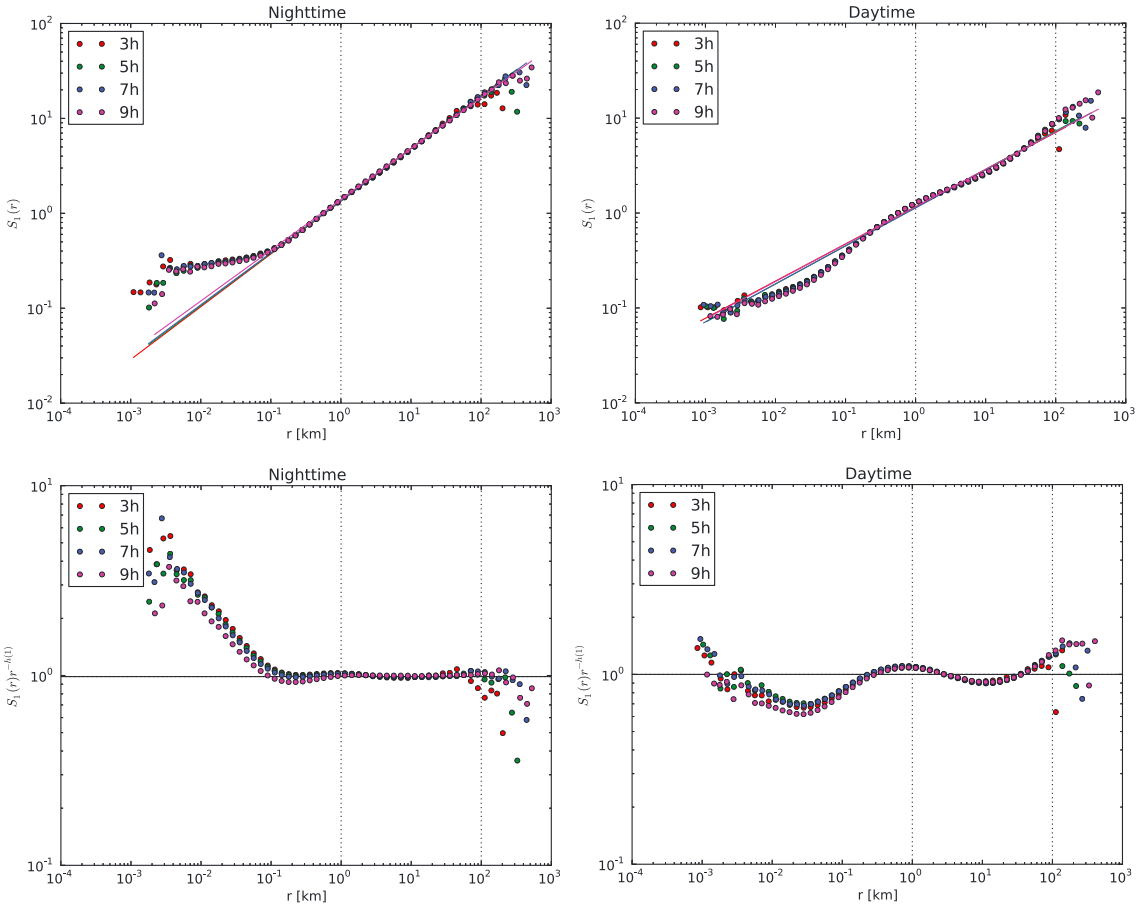

Figure 5. Plots of the first-order structure functions $S_1(r)$ for (top left) nocturnal residual layer and (top right) daytime convective mixed layer regimes. Each curve has been normalized by its value at $r = 10$ km. The best fitting power laws are shown as solid lines. Vertical dotted lines indicate the least squares fitting region. The normalized first-order structure function $S_1(r)/r^H$ for (bottom left) nocturnal residual layer and (bottom right) daytime convective mixed layer regimes. Colored symbols denote the length of analysis periods as defined in Table 1.

power law behavior evident in the nontruncated structure functions is likely related to nonstationarity that is removed by detrended fluctuation analysis. Plots of F_1/r^{H+1}, as were shown for the truncated fluctuation function in Figure 4, are shown in Figure 6 for nontruncated detrended fluctuation functions.

4.3. Computed Scaling Exponents

Tables 2 and 3 report the scaling exponent H estimated by structure function analysis and detrended fluctuation analysis for the residual layer and convective boundary layer cases. Also reported in the tables are the 95% confidence interval for the least squares slope parameter. The narrowness of the 95% confidence interval has been proposed as an indicator of the existence of power law behavior, although what defines sufficient narrowness is ad hoc [e.g., *Tuck*, 2010]. In order to avoid specifying an ad hoc parameter, the numerical values of the confidence interval are given in Tables 2 and 3.

The results for the nocturnal residual layer are shown in Table 2. In all cases $H > 0.5$, with the range of H for all cases being $0.518 \leq H \leq 0.578$. There is some evidence that H becomes smaller as the length of the temporal subset increases, although this increase is relatively small. The detrended fluctuation analysis estimates for H are in general slightly larger than the structure function estimates; however, this difference is again rather small. The 95% confidence intervals are generally more narrow for the detrended fluctuation estimates than for the structure function estimates, indicating that the detrended fluctuation estimates can be more closely fit by a power law relationship.

In the convective mixed layer the range of H for all cases is $0.297 \leq H \leq 0.403$. The 95% confidence intervals indicate that the structure functions and detrended fluctuation functions are well fit by a power law in all cases. There is a larger difference in H between truncated and nontruncated structure functions than

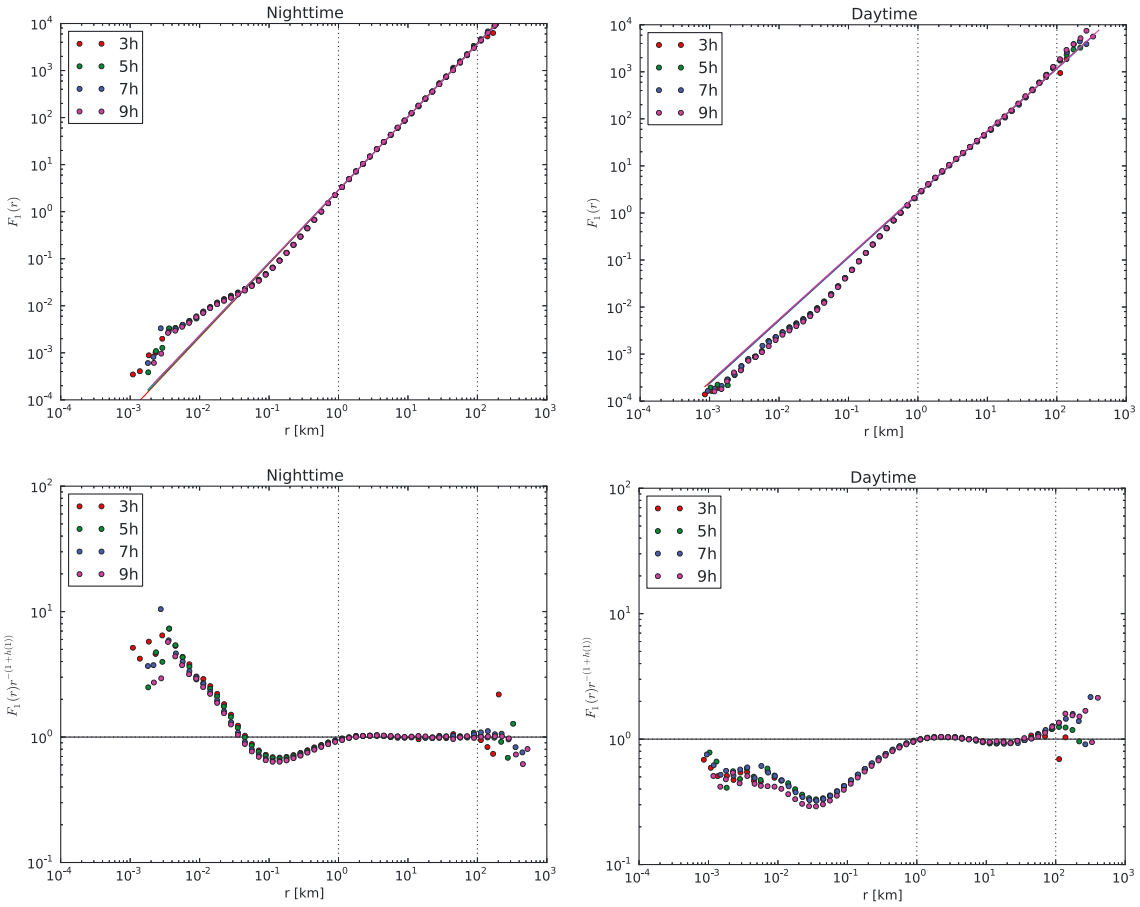

Figure 6. Plots of the detrended fluctuation functions $F_1(r)$ for (top left) nocturnal residual layer and (top right) convective mixed layer regimes. Each curve has been normalized by its value at $r = 10$ km. The best fitting power laws are shown as solid lines. Vertical dotted lines indicate the least squares fitting region. The normalized detrended fluctuation functions $F_1(r)/r^{H+1}$ for (bottom left) nocturnal residual layer and (bottom right) daytime convective mixed layer regimes. Colored symbols denote the length of analysis periods as defined in Table 1.

for truncated and nontruncated detrended fluctuation functions. This suggests that nonstationarity may be affecting the structure functions in the convective mixed layer and that greater confidence should be placed in the detrended fluctuation estimate of H than in the structure function. This nonstationarity of the convective mixed layer is not surprising given the larger daytime nonstationarity in other daytime boundary layer properties. In both truncated and nontruncated cases the detrended fluctuation estimates of H are remarkably close to $H = \frac{1}{3}$, with the nontruncated case lying closest to that value.

In Table 4 the results of the structure function analysis of water vapor fields observed by the Atmospheric Infrared Sounder (AIRS) reported previously in PC12 are reproduced alongside the nontruncated detrended fluctuation analysis results for the 9 h subset length. The results for the WLEF analysis shown in Table 4 have been limited to nontruncated detrended fluctuation analysis results for the 9 h subset length, because this

Table 2. Scaling Exponents H and 95% Confidence Intervals for the Residual Layer[a]

Length (h)	Night SF $N_s/4$	Night SF N_s	Night DFA $N_s/4$	Night DFA N_s
3	0.537 ± 0.0138	0.556 ± 0.012	0.560 ± 0.012	0.563± 0.008
5	0.552 ± 0.008	0.552 ± 0.008	0.578 ± 0.009	0.558 ± 0.006
7	0.538 ± 0.011	0.548 ± 0.007	0.550 ± 0.0154	0.546 ± 0.007
9	0.518 ± 0.021	0.535 ± 0.001	0.535 ± 0.0217	0.548 ± 0.009

[a]The scaling exponents are reported for both the structure function (denoted SF) and detrended fluctuation function (denoted DFA) methodologies. N_s and $N_s/4$ indicate untruncated and truncated results, respectively.

Table 3. Scaling Exponents H and 95% Confidence Intervals for the Convective Mixed Layer[a]

Length (h)	Day SF $N_s/4$	Day SF N_s	Day DFA $N_s/4$	Day DFA N_s
3	0.297 ± 0.029	0.392 ± 0.02	0.362 ± 0.013	0.334 ± 0.018
5	0.310 ± 0.015	0.403 ± 0.033	0.328 ± 0.018	0.341 ± 0.023
7	0.335 ± 0.022	0.400 ± 0.031	0.348 ± 0.025	0.337 ± 0.024
9	0.337 ± 0.027	0.394 ± 0.029	0.329 ± 0.022	0.334 ± 0.018

[a]The scaling exponents are reported for both the structure function (denoted SF) and detrended fluctuation function (denoted DFA) methodologies. N_s and $N_s/4$ indicate untruncated and truncated results, respectively.

case allows the largest range of scales to be investigated and by use of detrended fluctuation analysis is less affected by potential nonstationarity. It is important to note that because the values reported from PC12 are for scaling exponents computed from a land-masked data set from ascending (daytime) satellite passes, the comparison between WLEF and AIRS data sets is not direct. The primary motivation for selecting this particular subset of AIRS data is the fact that the empirical averaging kernels reported in PC12 suggest that AIRS is most sensitive to boundary layer water vapor during ascending passes over the ocean. Nonetheless, there is considerable agreement between the estimates of H from the AIRS and WLEF analysis, especially given the substantial differences in the observational techniques. However, it is important to distinguish between the range of scales over which the two analyses were performed. The range of scales considered in the present analysis extend from 1 km to 100 km. The range of scales considered in the AIRS analysis, described in PC12, extends from 50 km to 500 km. Therefore, the scaling exponents H computed between the two studies are not a direct comparison; however, agreement in the scaling exponents between the two studies provides evidence that a single scaling exponent characterizes the scale invariance of atmospheric water vapor structure functions and spectra over the full range of scales from 1 km to 500 km.

Perhaps the most surprising aspect of the results shown in Table 4 is the agreement between the AIRS free tropospheric and WLEF residual layer estimates of H. This is particularly the case given that the AIRS free tropospheric estimate is computed from AIRS retrievals at the 500 hPa level, which is without question (based upon the empirical averaging kernels shown in PC12) representative of the free troposphere, while the WLEF residual layer case is representative of observations made at a height that without question (and in fact by definition) undergoes substantial variations on a diurnal time scale. Hence, the dynamical processes operating between the two cases would be expected to be substantially different, yet they are nonetheless characterized by very similar scaling exponents. Without further observations of the residual layer and free troposphere, it is difficult to surmise why there should be such agreement. Perhaps the strongest similarity between the free troposphere and residual layer is that in both cases the flow field is largely two-dimensional and is not being actively mixed by buoyant convection.

Table 4. A Comparison of H Computed From AIRS Observations to Those Computed From WLEF Time Series[a]

Regime	AIRS JJA ASC	AIRS DJF ASC	WLEF
FT (RL)	0.548 ± 0.002	0.556 ± 0.002	0.548 ± 0.009
BL (ML)	0.334 ± 0.002	0.335 ± 0.002	0.334 ± 0.018

[a]The AIRS observations are reported for ascending (daytime) passes during June, July, and August (JJA) and for December, January, and February (DJF) for both free tropospheric (500 hPa) and boundary layer (925 hPa) regimes reproduced from PC12. AIRS H are computed based upon land-masked data sets. The free troposphere and boundary layer regimes are denoted as FT and BL, respectively. For the AIRS analysis H is determined over scales ranging from 50 km to 500 km. The AIRS scaling exponents are given as reported in PC12. For the WLEF analysis H is determined over scales ranging from 1 km to 100 km. The WLEF results based upon DFA of 9 h time series are given for the residual layer (RL) and mixed layer (ML) separately.

There is also striking agreement between the AIRS boundary layer (925 hPa) and WLEF convective mixed layer scaling exponents. This result provides strong evidence of $H \approx \frac{1}{3}$ scaling between 1 km and 500 km and is in general agreement with the findings of *Cho et al.* [1999a], *Wood and Taylor* [2001], *Comstock et al.* [2005], *Kahn et al.* [2011], and *Fischer et al.* [2012]. It is important to note that the 925 hPa scaling exponents reported in PC12 do not undergo as pronounced of a diurnal cycle as is seen in this study. This is not surprising given that the results reported in PC12 are computed from land-masked data and a weaker boundary layer diurnal cycle would be expected over the ocean. What sets the results reported here apart from these prior studies is the size of the

data set that has been analyzed, the efforts that have been made to reduce errors in the analysis methodology, and the estimated error bars on the quantitative estimates of H. Together these three properties allow greater confidence in statements regarding the universality of $H \approx \frac{1}{3}$ as characterizing the spatial scale dependence of first-order statistical variability in the boundary layer at scales up to 500 km.

5. Summary and Conclusions

This work has shown that the first-order structure function and detrended fluctuation function of the water vapor field exhibit approximate power law behavior at scales between 1 km and 100 km within the convective mixed layer and nocturnal residual layer. Detrended fluctuation functions are shown to more closely follow a power law relationship than structure functions, although only slightly. Using least squares, it is shown that the Hurst exponents H for the residual layer and convective mixed layer are estimated to be $H = 0.548 \pm 0.009$ and $H = 0.334 \pm 0.018$, respectively. The estimate of H for the residual layer is shown to be in very close agreement with the estimates of H for the free troposphere from the AIRS analysis. Similarly, the estimate of H for the convective mixed layer is shown to be in very close agreement with the estimate of H for the maritime boundary layer from AIRS. Finally, the near equality of H for the AIRS boundary layer regime with H for the WLEF convective mixed layer, when interpreted in the context of previous results, offers support for the universality of $H \approx \frac{1}{3}$ in the convectively mixed boundary layer.

The rapid transition of scaling exponents from $H \approx \frac{1}{3}$ in the convective mixed layer to $H > \frac{1}{2}$ in the residual layer seem to support the hypothesized role of buoyant convective motions in establishing the convective mixed layer spectra over relatively short time scales as proposed by *Fischer et al.* [2012, 2013] and PC12. In the residual layer, support for a particular physical explanation for the observed spectral scaling is not as apparent, although it seems likely that the near two-dimensionality of the mixing processes and the potential role of long-range transport are a starting point.

The results underscore the need for further exploration of the vertical variability of water vapor scaling exponents in the lower troposphere and in particular the nocturnal residual layer. High-resolution vertically resolved observations of the free troposphere and residual layer are becoming more practical as has been shown by *Fischer et al.* [2012, 2013] using airborne lidar. Numerical studies may also prove fruitful, although simulations with domains of sufficient extent to support water vapor fluctuations with horizontal scales of 500 km but with sufficient resolution to resolve the complicated dynamics of the stable boundary layer are unlikely to be realized in the near future.

Despite uncertainties in establishing a precise physical or theoretical explanation for the observed scaling, the results presented in this work should lend additional confidence to the growing consensus of $H = \frac{1}{3}$ scaling of water vapor spectra in the boundary layer and therefore lend confidence to its use as an empirical basis for the construction of parameterizations for numerical models.

Acknowledgments

This research was supported by the Director, Office of Science, Office of Biological and Environmental Research of the U.S. Department of Energy under contract DE-AC02-05CH11231 as part of their Regional and Global Climate Modeling Program. Observations at the WLEF Park Falls Ameriflux site are supported by National Science Foundation (NSF) DEB-0845166, the Department of Energy Lawrence Berkeley National Lab Ameriflux Network Management Project, and NOAA Earth Systems Research Lab. These observations were made with the assistance of Jonathan Thom, University of Wisconsin-Madison; Arlyn Andrews, NOAA ESRL; Jonathan Kofler, NOAA ESRL; and Dan Buamann, U.S. Geological Survey. We are grateful for support by the Terrestrial Hazard Observation and Reporting (THOR) Center at Caltech and by the National Science Foundation (grant ARC-1107795). The flux and meteorological data from the WLEF tower are free, fair use, and available online at http://flux.aos.wisc.edu/twiki/bin/view/Main/ChEASData and also archived at the Fluxnet/Ameriflux repository. The high-frequency WLEF tower observations used in this study are available online at http://flux.aos.wisc.edu/data/wlef/2013JD021141.

References

Berger, B., K. Davis, C. Yi, P. Bakwin, and C. Zhao (2001), Long-term carbon dioxide fluxes from a very tall tower in a northern forest: Flux measurement methodology, *J. Atmos. Oceanic Technol.*, *18*(4), 529–542.

Bretherton, C., P. Blossey, and M. Khairoutdinov (2005), An energy-balance analysis of deep convective self-aggregation above uniform SST, *J. Atmos. Sc.*, *26*(12), 4273–4292, doi:10.1175/JAS3614.1.

Brown, P., and G. Robinson (1979), The variance spectrum of tropospheric winds over eastern Europe, *J. Atmos. Sci.*, *36*(2), 270–286.

Charney, J. (1971), Geostrophic turbulence, *J. Atmos. Sci.*, *28*, 1087–1094.

Cho, J., R. Newell, and J. Barrick (1999a), Horizontal wavenumber spectra of winds, temperature, and trace gases during the Pacific exploratory missions: 1. Climatology, *J. Geophys. Res.*, *104*(D5), 5697–5716.

Cho, J., R. Newell, and J. Barrick (1999b), Horizontal wavenumber spectra of winds, temperature, and trace gases during the Pacific exploratory missions: 2. Gravity waves, quasi-two-dimensional turbulence, and vortical modes, *J. Geophys. Res.*, *104*(D13), 16,297–16,308.

Cho, J., R. Newell, and G. Sachse (2000), Anomalous scaling of mesoscale tropospheric humidity fluctuations, *Geophys. Res. Lett.*, *27*(3), 377–380.

Comstock, K., C. Bretherton, and S. Yuter (2005), Mesoscale variability and drizzle in southeast Pacific stratocumulus, *J. Atmos. Sci.*, *62*(10), 3792–3807.

Cusack, S., J. Edwards, and R. Kershaw (1999), Estimating the subgrid variance of saturation, and its parametrization for use in a GCM cloud scheme, *Q. J. R. Meteorol. Soc.*, *125*(560), 3057–3076.

Davis, K., P. Bakwin, C. Yi, B. Berger, C. Zhao, R. Teclaw, and J. Isebrands (2003), The annual cycles of CO_2 and H_2O exchange over a northern mixed forest as observed from a very tall tower, *Global Change Biol.*, *9*(9), 1278–1293.

de Roode, S., P. Duynkerke, and H. Jonker (2004), Large-eddy simulation: How large is large enough?, *J. Atmos. Sci.*, *61*(4), 403–421.

Fischer, L., C. Kiemle, and G. C. Craig (2012), Height-resolved variability of midlatitude tropospheric water vapor measured by an airborne lidar, *Geophys. Res. Lett.*, *39*, L06803, doi:10.1029/2011GL050621.

Fischer, L., G. C. Craig, and C. Kiemle (2013), Horizontal structure function and vertical correlation analysis of mesoscale water vapor variability observed by airborne lidar, *J. Geophys. Res. Atmos.*, *118*(14), 7579–7590, doi:10.1002/jgrd.50588.
Gage, K. S., and G. D. Nastrom (1986), Theoretical interpretation of atmospheric wavenumber spectra of wind and temperature observed by commercial aircraft during gasp, *J. Atmos. Sci.*, *43*(7), 729–740.
Gifford, F. (1956), The relation between space and time correlations in the atmosphere, *J. Meteorol.*, *13*(3), 289–294.
Gossard, E. (1960), Power spectra of temperature, humidity and refractive index from aircraft and tethered balloon measurements, *IRE Trans. Anntenas Propag.*, *8*(2), 186–201.
Holton, J. (2004), *An Introduction to Dynamic Meteorology*, Academic Press, Burlington, Mass.
Ivanova, K., and M. Ausloos (1999), Application of the detrended fluctuation analysis (DFA) method for describing cloud breaking, *Physica A*, *274*(1), 349–354.
Ivanova, K., M. Ausloos, E. Clothiaux, and T. Ackerman (2000), Break-up of stratus cloud structure predicted from non-Brownian motion liquid water and brightness temperature fluctuations, *Europhys. Lett.*, *52*, 40–46.
Kahn, B., and J. Teixeira (2009), A global climatology of temperature and water vapor variance scaling from the atmospheric infrared sounder, *J. Clim.*, *22*(20), 5558–5576.
Kahn, B., et al. (2011), Temperature and water vapor variance scaling in global models: Comparisons to satellite and aircraft data, *J. Atmos. Sci.*, *68*(9), 2156–2168.
Kantelhardt, J., S. Zschiegner, E. Koscielny-Bunde, S. Havlin, A. Bunde, and H. Stanley (2002), Multifractal detrended fluctuation analysis of nonstationary time series, *Physica A*, *316*(1), 87–114.
Kavasseri, R., and R. Nagarajan (2005), A multifractal description of wind speed records, *Chaos, Solitons Fractals*, *24*(1), 165–173.
Koscielny-Bunde, E., A. Bunde, S. Havlin, H. E. Roman, Y. Goldreich, and H.-J. Schellnhuber (1998), Indication of a universal persistence law governing atmospheric variability, *Phys. Rev. Lett.*, *81*, 729–732.
Lappe, U., and B. Davidson (1963), On the range of validity of Taylor's hypothesis and the Kolmogoroff spectral law, *J. Atmos. Sci.*, *20*(6), 569–576.
Larson, V., R. Wood, P. Field, J. Golaz, T. Vonder Haar, and W. Cotton (2001), Systematic biases in the microphysics and thermodynamics of numerical models that ignore subgrid-scale variability, *J. Atmos. Sci.*, *58*(9), 1117–1128.
Larson, V. E., D. P. Schanen, M. Wang, M. Ovchinnikov, and S. Ghan (2012), PDF parameterization of boundary layer clouds in models with horizontal grid spacings from 2 to 16 km, *Mon. Weather Rev.*, *140*, 285–306, doi:10.1175/MWR-D-10-05059.1.
Leung, Y. (2010), *Knowledge Discovery in Spatial Data*, Springer, New York.
Li, Z., and Y. Zhang (2007), Quantifying fractal dynamics of groundwater systems with detrended fluctuation analysis, *J. Hydrol.*, *336*(1), 139–146.
L'vov, V. S., A. Pomyalov, and I. Procaccia (1999), Temporal surrogates of spatial turbulent statistics: The Taylor hypothesis revisited, *Phys. Rev. E*, *60*, 4175–4184, doi:10.1103/PhysRevE.60.4175.
Mackay, D., D. Ahl, B. Ewers, S. Gower, S. Burrows, S. Samanta, and K. Davis (2002), Effects of aggregated classifications of forest composition on estimates of evapotranspiration in a northern wisconsin forest, *Global Change Biol.*, *8*(12), 1253–1265.
Matsoukas, C., S. Islam, and I. Rodriguez-Iturbe (2000), Detrended fluctuation analysis of rainfall and streamflow time series, *J. Geophys. Res.*, *105*(D23), 29,165–29,172.
Nastrom, G., and K. Gage (1985), A climatology of atmospheric wavenumber spectra of wind and temperature observed by commercial aircraft, *J. Atmos. Sci.*, *42*(9), 950–960.
Peng, C.-K., S. V. Buldyrev, S. Havlin, M. Simons, H. E. Stanley, and A. L. Goldberger (1994), Mosaic organization of DNA nucleotides, *Phys. Rev. E*, *49*, 1685–1689.
Pope, S. (2000), *Turbulent Flows*, Cambridge Univ. Press, Cambridge, U. K.
Pressel, K. G., and W. D. Collins (2012), First-order structure function analysis of statistical scale invariance in the AIRS-observed water vapor field, *J. Clim.*, *25*(16), 5538–5555, doi:10.1175/JCLI-D-11-00374.1.
Skamarock, W. C. (2004), Evaluating mesoscale NWP models using kinetic energy spectra, *Mon. Weather Rev.*, *132*(12), 3019–3032.
Talkner, P., and R. Weber (2000), Power spectrum and detrended fluctuation analysis: Application to daily temperatures, *Phys. Rev. E*, *62*(1), 150–160.
Taylor, G. I. (1935), Statistical theory of turbulence, *Proc. R. Soc. London, Ser. A*, *151*(873), 421–444.
Tuck, A. (2010), From molecules to meteorology via turbulent scale invariance, *Q. J. R. Meteorol. Soc.*, *136*(650), 1125–1144.
Varotsos, C. A., J. M. Ondov, A. P. Cracknell, M. N. Efstathiou, and M. N. Assimakopoulos (2006), Long-range persistence in global aerosol index dynamics, *Int. J. Remote Sens.*, *27*(16), 3593–3603, doi:10.1080/01431160600617236.
Wood, R., and D. L. Hartmann (2006), Spatial variability of liquid water path in marine low cloud: The importance of mesoscale cellular convection, *J. Clim.*, *19*(9), 1748–1764.
Wood, R., and J. P. Taylor (2001), Liquid water path variability in unbroken marine stratocumulus cloud, *Q. J. R. Meteorol. Soc.*, *127*(578), 2635–2662.
Yi, C., K. Davis, B. Berger, and P. Bakwin (2001), Long-term observations of the dynamics of the continental planetary boundary layer, *J. Atmos. Sci.*, *58*(10), 1288–1299.
Zhang, Q., C. Xu, Y. Chen, and Z. Yu (2008), Multifractal detrended fluctuation analysis of streamflow series of the Yangtze River basin, China, *Hydrol. Processes*, *22*(26), 4997–5003.
Zhao, C., P. Bakwin, and P. Tans (1997), A design for unattended monitoring of carbon dioxide on a very tall tower, *J. Atmos. Oceanic Technol.*, *14*(5), 1139–1145.